



## Enhanced thermodynamic stability and carrier lifetime in BF<sub>4</sub>-doped wide-band-gap perovskite solar cells

Zhong-Yuan Wang <sup>1,2</sup>, Kai-Feng Wang,<sup>1</sup> Jun-Jie Jin,<sup>1</sup> Fangping Ouyang,<sup>1,2</sup> Biao Meng,<sup>2</sup> Zhaofeng Wu,<sup>2</sup> Li-Min Liu,<sup>3</sup> and Chuan-Jia Tong <sup>1,2,\*</sup>

<sup>1</sup>*Institute of Quantum Physics, Hunan Key Laboratory of Nanophotonics and Devices, Hunan Key Laboratory of Super-Microstructure and Ultrafast Process, School of Physics, Central South University, Changsha 410083, China*

<sup>2</sup>*School of Material Science and Engineering, Xinjiang University, Urumqi, Xinjiang 830046, China*

<sup>3</sup>*School of Physics, Beihang University, Beijing 100191, China*



(Received 14 May 2024; revised 1 July 2024; accepted 8 July 2024; published 23 July 2024)

Recent experiments show that doping a small amount of fluorinated pseudohalides (BF<sub>4</sub>) into CH<sub>3</sub>NH<sub>3</sub>PbI<sub>3</sub> (MAPbI<sub>3</sub>) can enhance the performance of wide-band-gap (WBG) perovskite solar cells. Using time-domain density functional theory and *ab initio* nonadiabatic molecular dynamics we demonstrate that BF<sub>4</sub>-doped WBG perovskites not only maintain the high defect tolerance but also exhibit greatly improved thermodynamic stability due to enhanced dissociation energy and reduced thermal atomic fluctuation. The strengthened hydrogen bond network introduces increased lattice rigidity, confined inner space, and the reorientated dipole direction of methylammonium molecules, which synergistically suppress the ion migration in BF<sub>4</sub>-doped MAPbI<sub>3</sub> perovskite. Notably, the charge carrier lifetime experiences an order-of-magnitude improvement after BF<sub>4</sub> doping, which is mainly attributed to the weakened nonadiabatic coupling. This work provides valuable insights into the effect of fluorinated pseudohalides doped in perovskite materials and suggests a promising approach to enhancing the stability and efficiency of WBG perovskite solar cells.

DOI: [10.1103/PhysRevB.110.045142](https://doi.org/10.1103/PhysRevB.110.045142)

### I. INTRODUCTION

Organic-inorganic hybrid perovskites (OIHPs), such as CH<sub>3</sub>NH<sub>3</sub>PbI<sub>3</sub> (MAPbI<sub>3</sub>), have emerged as outstanding photovoltaic materials owing to their impressive electronic and optical properties, which include an ideal energy band, excellent charge transport capability, high defect tolerance, and low cost [1–6]. These outstanding photovoltaic properties have boosted the power conversion efficiencies (PCEs) of OIHP solar cells, achieving 26% within a decade [7]. To further enhance the performance of perovskite solar cells (PSCs) and surpass the efficiency limit of single-junction photovoltaics, a promising approach involves the construction of all-perovskite tandem solar cells. The state of the art all-perovskite tandem solar cell, which includes a wide-band-gap (WBG) perovskite with a band gap of 1.78 eV, has been certified for a remarkable efficiency of 28.50% [8], exceeding the efficiency of the best-performing single-junction PSCs [7] and other solar cells [9,10]. Adjusting the ratio of iodide (I) and bromide (Br) in perovskite materials allows for tuning of the band gap [11,12], but a high concentration of Br introduces stability issues and performance degradation [13–16].

The introduction of additives, such as Lewis adducts, amino acids, and pseudohalogens, has been identified as an effective way to enhance the performance and stability of the WBG perovskite devices [17–22]. Recently, fluorinated pseudohalides have emerged as promising anion substitutes due to their higher electronegativity compared to traditional halides

[23]. Among them, tetrafluoroborate (BF<sub>4</sub><sup>−</sup>) has recently been doped in the WBG perovskite systems as it shares similar chemical properties and an ionic radius with I<sup>−</sup> [24,25]. Tao *et al.* demonstrated that substituting a small amount of I<sup>−</sup>/Br<sup>−</sup> anions with BF<sub>4</sub><sup>−</sup> in PSCs reduced the density of trap states, and thereby inhibited phase separation and carrier recombination [21]. Su *et al.* found that doping BF<sub>4</sub> into a Br-doped WBG mixed halide perovskite led to reduced trap density and eliminated ion migration channels, thereby achieving high device performance [20]. Koh *et al.* reported that doping BF<sub>4</sub> ions on the surface of WBG perovskite effectively passivated the surface defects and, consequently, enhanced the open-circuit voltage (V<sub>OC</sub>) [26]. However, the intrinsic relationship between BF<sub>4</sub> doping and the superior stability and efficiency of WBG PSCs is not yet fully understood. Particularly, it is still unclear whether BF<sub>4</sub> doping still maintains the high defect tolerance like pure MAPbI<sub>3</sub> perovskites and why BF<sub>4</sub> doping reduces defect density and improves carrier lifetime. Therefore, further theoretical studies on underlying microscopic mechanisms in BF<sub>4</sub>-doped WBG PSCs are required.

In this study, both time-independent and real-time time-dependent density functional theory (TDDFT) simulations show that MAPbI<sub>3-x</sub>(BF<sub>4</sub>)<sub>x</sub> systems, when doped with low BF<sub>4</sub> concentrations, exhibit several advantages over pure MAPbI<sub>3</sub>. Notably, BF<sub>4</sub> doping strongly enhances the dissociation energy and reduces the thermal atomic fluctuation in MAPbI<sub>3-x</sub>(BF<sub>4</sub>)<sub>x</sub>, suggesting better thermodynamic stability and easier stoichiometric phase formation than in undoped MAPbI<sub>3</sub>. Furthermore, these BF<sub>4</sub>-doped systems do not introduce additional deep energy level defects, thereby

\*Contact author: [chuanjia.tong@csu.edu.cn](mailto:chuanjia.tong@csu.edu.cn)

maintaining the high defect tolerance characteristic observed in pure MAPbI<sub>3</sub> perovskite. Strong N–H···F hydrogen bonds and adjacent strengthened N–H···I hydrogen bonds are formed in BF<sub>4</sub>-doped MAPbI<sub>3</sub> perovskites, which reduce the anharmonicity of the soft inorganic lattice, introduce the spatial confinement effect, and induce the reorientation of dipole direction due to methylammonium (MA) molecules. These factors synergistically suppress the most popular iodine migration, thereby inhibiting the common issue of phase separation in halogen-doped WBG perovskites and contributing to enhanced long-term stability. Moreover, nonadiabatic molecular dynamics (NAMD) simulations demonstrate that both nonradiative electron-hole (*e*–*h*) recombination and hot carrier (HC) cooling processes are greatly suppressed after BF<sub>4</sub> doping mainly due to the significantly weakened nonadiabatic coupling (NAC). Finally, a 10% delocalized BF<sub>4</sub>-doped MAPbI<sub>3</sub> shows significant potential for its application as the top cell in all-perovskite tandem solar cells. The reported results rationalize the benefits of BF<sub>4</sub>-doped MAPbI<sub>3</sub> in WBG PSCs and highlight the role of low concentration of BF<sub>4</sub> doping in enhancing the stability and efficiency of these solar cells.

## II. SIMULATION METHODOLOGY

The electronic structure and molecular dynamics (MD) trajectories were obtained using density-functional theory (DFT) as implemented in the Vienna *ab initio* simulation package (VASP) [27]. The exchange-correlation interactions were described using the Perdew-Burke-Ernzerhof (PBE) functional [28] while the electron-ion interactions were treated using the projector-augmented wave (PAW) method [29]. The primitive unit cell contains four MAPbI<sub>3</sub> formula units, comprising 48 atoms. All systems are based on a 2 × 2 × 2 supercell of tetragonal MAPbI<sub>3</sub>, containing 384 or more atoms in the MAPbI<sub>3-x</sub>(BF<sub>4</sub>)<sub>x</sub> structures. The doping percentages of 2%, 6%, and 10% BF<sub>4</sub> correspond to replacing two, four, and ten iodine ions with BF<sub>4</sub> ions, respectively. A plane-wave energy cutoff of 500 eV was set, and geometry optimization was performed using a Gamma scheme *k*-point mesh. Geometry optimization was terminated when ion forces fell below 2 × 10<sup>-2</sup> eV/Å. The reaction coordinates and the activation energies were calculated with the climbing image nudged elastic band (CINEB) method [30,31]. Van der Waals interactions were considered using the Grimme DFT-D3 method, incorporating the Becke-Johnson damping function [32,33]. To investigate the *e*–*h* recombination process, NAMD was conducted using the semiclassical decoherence-induced surface hopping (DISH) approach [34], as implemented in the PYXAID software package [35,36]. This method has been used successfully to study excited-state dynamics in a variety of perovskite systems and other materials [37–42]. More theory details on NAMD can be found in the Supplemental Material [43] (see also Refs. [44–49] therein).

The formation enthalpies  $\Delta H_f(\alpha, q)$  of a complex defect in the charge state *q* using the supercell model can be expressed as [50,51]

$$\Delta H_f(\alpha, q) = E(\alpha, q) - E(\text{host}) + \sum n_i(\mu_i + \Delta\mu_i) + q[E_{\text{VBM}}(\text{host}) + E_F + \Delta V], \quad (1)$$

where  $E(\alpha, q)$  and  $E(\text{host})$  are the total energies of the supercell with and without defects, respectively.  $n_i$  is the number of *i* atoms added ( $n_i < 0$ ) or removed ( $n_i > 0$ ). In this equation,  $\mu_i$  represents the chemical potential of *i* atoms,  $\Delta\mu_i$  denotes the permissible variation in chemical potential, and  $q$  is the number of electrons transferred from the supercell to the reservoirs during the defect cell formation. Here,  $E_{\text{VBM}}$  is the energy of the valence band maximum (VBM) of the pristine supercell, while  $E_F$  is the Fermi energy referenced to the VBM level. The term  $\Delta V$  represents correction for both electrostatic potential alignment and finite-size effects in charged systems. The thermodynamic charge transition levels, denoted as  $\varepsilon(q/q')$ , correspond to the  $E_F$  where the formation energy  $\Delta H_f(\alpha, q) = \Delta H_f(\alpha, q')$  for a defect  $\alpha$  with different charge state *q* and  $q'$ :

$$\varepsilon(q/q') = [E(\alpha, q) - E(\alpha, q') + (q - q')(E_{\text{VBM}} + \Delta V)] / (q - q'). \quad (2)$$

## III. RESULTS AND DISCUSSION

Figure 1(a) shows the most stable tetragonal phase of pure MAPbI<sub>3</sub> at room temperature. Previous experimental work has shown that low concentration with no more than 10% of BF<sub>4</sub> doping is particularly beneficial to the perovskite performance [52]. Particularly, the band gap of 10% BF<sub>4</sub>-doped MAPbI<sub>3</sub> is 1.78 eV as shown in Table II, making it a promising candidate for WBG perovskite. Thus several representative models of MAPbI<sub>3-x</sub>(BF<sub>4</sub>)<sub>x</sub> WBG perovskite, doped with BF<sub>4</sub> at low concentrations (2%, 6%, and 10%), are selected in this work. Figures 1(c)–1(f) depict the optimized structure of pure MAPbI<sub>3</sub> perovskite and three different BF<sub>4</sub>-doped systems, respectively. Only a slight lattice expansion has been observed upon doping with a small amount of BF<sub>4</sub>, as demonstrated in Fig. S1 in the Supplemental Material [43]. However, in the 2%, 6%, and 10% BF<sub>4</sub>-doped systems, the MA molecules surrounding BF<sub>4</sub> experience a considerable reorientation as shown in Fig. 1(b). The reorientation leads to the formation of strong N–H···F hydrogen bonds with average bond lengths of 1.76, 1.81, and 1.80 Å, respectively, much shorter than the 2.78 Å of the average N–H···I hydrogen bond in pure MAPbI<sub>3</sub>. The strong hydrogen bond in BF<sub>4</sub>-doped perovskites should be attributed to the high electronegativity of fluorine when compared to iodine, since similar strong N–H···F hydrogen bonds have been found [53,54] in BF<sub>4</sub>-doped formamidinium (FA)-based perovskites. Moreover, the reorientation of MA induced by BF<sub>4</sub> doping can also strengthen the interaction between MA molecules and iodine atoms in adjacent layers, due to shortened N–H···I hydrogen bond lengths as illustrated in Figs. 1(d)–1(f) and Fig. S1 [43]. Such results indicate strong hydrogen bonds would spread throughout the whole structure after BF<sub>4</sub> doping. It is well known that the hydrogen bond plays a vital role in OIHPs, such as affecting crystal structure, charge transport, mechanical performance, etc. [55]. Particularly, the strong N–H···F and adjacent N–H···I hydrogen bonds would strengthen the interaction between the organic and inorganic framework, thereby enhancing the rigidity and stability of the soft perovskite lattice.

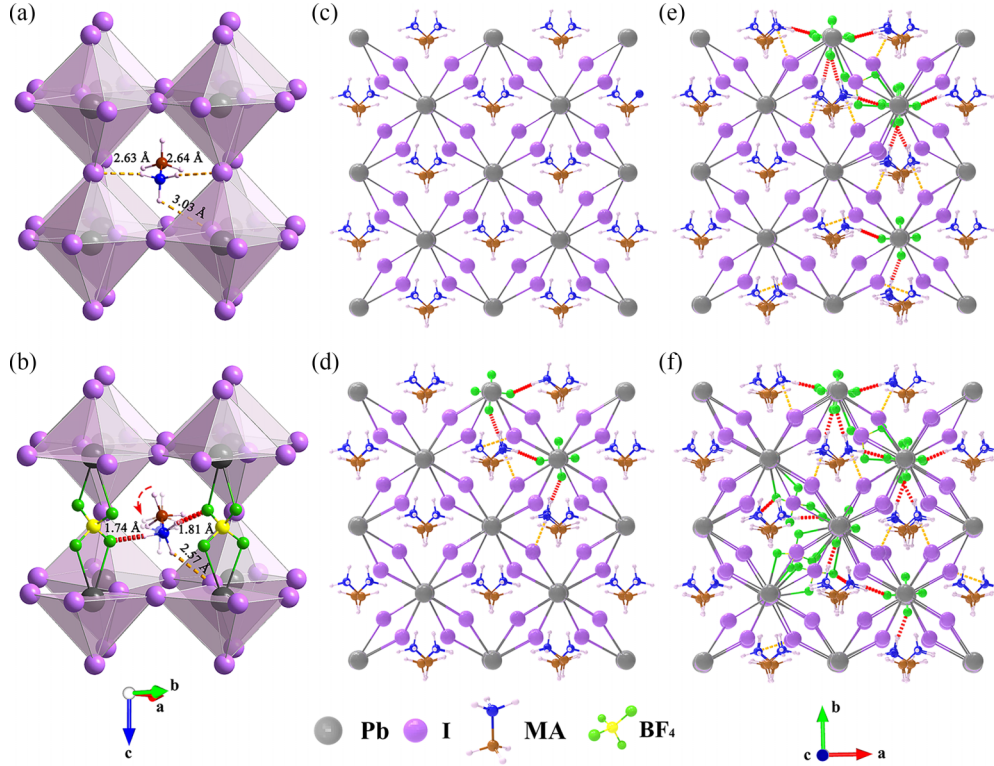


FIG. 1. Optimized partial structure of (a) pure MAPbI<sub>3</sub> and (b) representative BF<sub>4</sub>-doped MAPbI<sub>3</sub>. Top views of (c) pure MAPbI<sub>3</sub>, (d) 2% BF<sub>4</sub>-doped MAPbI<sub>3</sub>, (e) 6% BF<sub>4</sub>-doped MAPbI<sub>3</sub>, and (f) 10% BF<sub>4</sub>-doped MAPbI<sub>3</sub>. The color coding for atoms is as follows: I—purple, Pb—gray, C—brown, N—blue, B—yellow, F—green, and H—light pink. The light orange and red dashed lines stand for N—H...I and N—H...F hydrogen bonds, respectively.

MAPbI<sub>3</sub> perovskite has been reported to easily decompose into MAI and PbI<sub>2</sub> due to its low thermal stability [16,56,57]. To investigate the thermal stability of BF<sub>4</sub>-doped WBG perovskites, their phase diagrams are constructed as illustrated in Fig. 2. In thermodynamic equilibrium growth conditions, for pure, 2% BF<sub>4</sub>-doped, 6% BF<sub>4</sub>-doped, and 10% BF<sub>4</sub>-doped MAPbI<sub>3</sub> systems, the existence of MAPbI<sub>3-x</sub>(BF<sub>4</sub>)<sub>x</sub> should satisfy

$$\Delta\mu_{\text{MA}} + \Delta\mu_{\text{Pb}} + 3\Delta\mu_{\text{I}} = \Delta H(\text{MAPbI}_3) = -5.52 \text{ eV}, \quad (3)$$

$$\begin{aligned} \Delta\mu_{\text{MA}} + \Delta\mu_{\text{Pb}} + 2.94\Delta\mu_{\text{I}} + 0.06\Delta\mu_{\text{BF}_4} \\ = \Delta H[\text{MAPbI}_{2.94}(\text{BF}_4)_{0.06}] \\ = -5.80 \text{ eV}, \end{aligned} \quad (4)$$

$$\begin{aligned} \Delta\mu_{\text{MA}} + \Delta\mu_{\text{Pb}} + 2.82\Delta\mu_{\text{I}} + 0.18\Delta\mu_{\text{BF}_4} \\ = \Delta H[\text{MAPbI}_{2.80}(\text{BF}_4)_{0.18}] \\ = -6.36 \text{ eV}, \end{aligned} \quad (5)$$

$$\begin{aligned} \Delta\mu_{\text{MA}} + \Delta\mu_{\text{Pb}} + 2.70\Delta\mu_{\text{I}} + 0.30\Delta\mu_{\text{BF}_4} \\ = \Delta H[\text{MAPbI}_{2.70}(\text{BF}_4)_{0.30}] \\ = -6.94 \text{ eV}, \end{aligned} \quad (6)$$

where  $\Delta H[\text{MAPbI}_{3-x}(\text{BF}_4)_x]$  is the formation energy of MAPbI<sub>3-x</sub>(BF<sub>4</sub>)<sub>x</sub>. To exclude the possible secondary phases

such as PbI<sub>2</sub> and MAI, the following constraints must be also satisfied,

$$\Delta\mu_{\text{Pb}} + 2\Delta\mu_{\text{I}} < \Delta H(\text{PbI}_2) = -2.42 \text{ eV}, \quad (7)$$

$$\Delta\mu_{\text{MA}} + \Delta\mu_{\text{I}} < \Delta H(\text{MAI}) = -3.08 \text{ eV}, \quad (8)$$

$$\Delta\mu_{\text{MA}} + \Delta\mu_{\text{BF}_4} < \Delta H(\text{MABF}_4) = -6.45 \text{ eV}, \quad (9)$$

$$\Delta\mu_{\text{Pb}} + 2\Delta\mu_{\text{BF}_4} < \Delta H[\text{Pb}(\text{BF}_4)_2] = -7.96 \text{ eV}, \quad (10)$$

where  $\Delta H(\text{PbI}_2)$ ,  $\Delta H(\text{MAI})$ ,  $\Delta H(\text{MABF}_4)$ , and  $\Delta H[\text{Pb}(\text{BF}_4)_2]$  are the formation energies of PbI<sub>2</sub>, MAI, MABF<sub>4</sub>, and Pb(BF<sub>4</sub>)<sub>2</sub>, respectively.

The regions of accessible equilibrium chemical potential for MAPbI<sub>3-x</sub>(BF<sub>4</sub>)<sub>x</sub> satisfying Eqs. (3)–(10), are depicted in Fig. 2. For the BF<sub>4</sub> doping systems, the constraints of  $\Delta\mu_{\text{BF}_4}$ ,  $\Delta\mu_{\text{Pb}}$ , and  $\Delta\mu_{\text{I}}$  can be deduced from these equations. For  $\Delta\mu_{\text{BF}_4}$ , our calculations show that it should satisfy the constraint  $\Delta\mu_{\text{BF}_4} \leq -3.98 \text{ eV}$ . To investigate the effect of BF<sub>4</sub> doping on the stability of perovskite phase synthesis,  $\Delta\mu_{\text{BF}_4}$  is set at  $-3.98 \text{ eV}$  across all BF<sub>4</sub>-doped systems, attributable to its low doping concentration. The red, blue, yellow, and green regions represent phases of MAPbI<sub>3-x</sub>(BF<sub>4</sub>)<sub>x</sub>, MAI, PbI<sub>2</sub>, and MABF<sub>4</sub>, respectively. As shown in Fig. 2(a), the narrow and long red chemical range represents the growth conditions for synthesizing the MAPbI<sub>3</sub> phase under equilibrium conditions. The narrow shape is attributed to a low dissociation energy of 0.015 eV [58,59], which is required for decomposing MAPbI<sub>3</sub> into MAI and PbI<sub>2</sub>, defined as

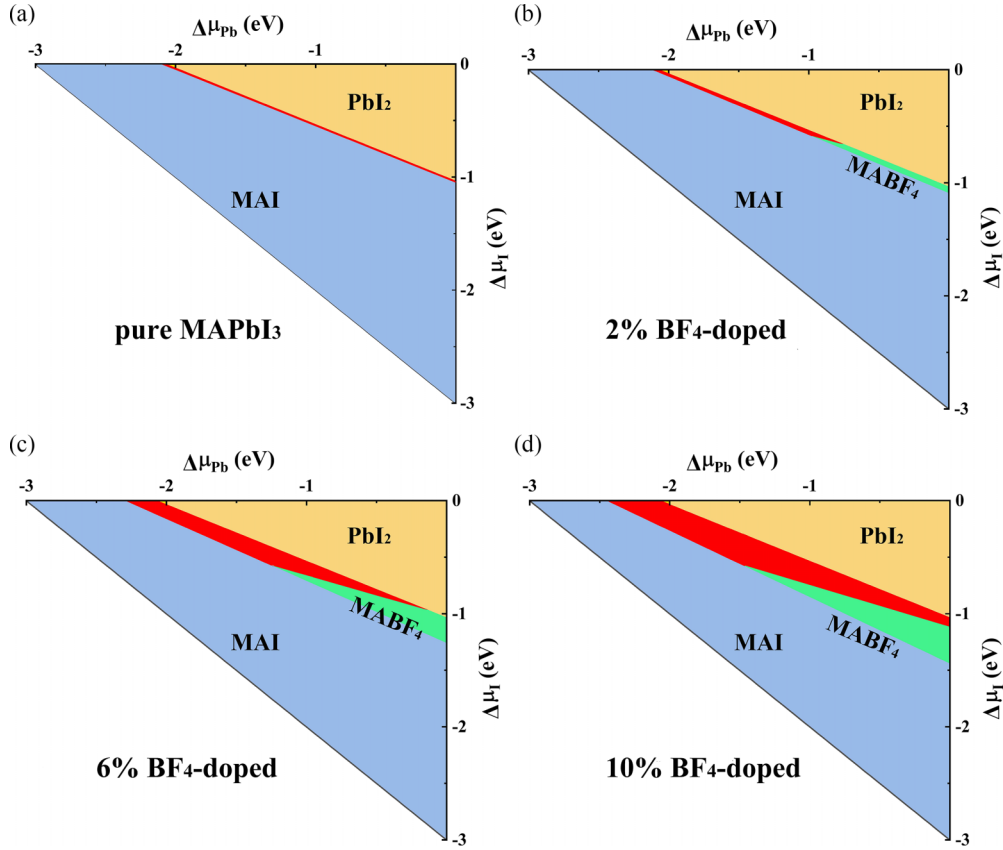


FIG. 2. The thermodynamic stable range for equilibrium growth of (a) pure MAPbI<sub>3</sub>, (b) 2% BF<sub>4</sub>-doped MAPbI<sub>3</sub>, (c) 6% BF<sub>4</sub>-doped MAPbI<sub>3</sub>, and (d) 10% BF<sub>4</sub>-doped MAPbI<sub>3</sub>, indicated by red. Outside this region, the compound will decompose into secondary phases.

$E(\text{MAI}) + E(\text{PbI}_2) - E(\text{MAPbI}_3)$ . Normally, the low dissociation energy indicates an easy decomposition into a secondary phase so that the growth conditions should be carefully controlled to form the stoichiometric MAPbI<sub>3</sub> perovskite. That is why traditional OIHs experience a low thermal stability issue. Interestingly, as the BF<sub>4</sub> doping concentration increases, the long red chemical range progressively widens as shown in Figs. 2(b)–2(d). The corresponding dissociation energies of 2%, 6%, and 10% BF<sub>4</sub>-doped perovskites progressively increase, reaching values of 0.14, 0.38, and 0.64 eV, respectively, an order of magnitude larger than that in pure MAPbI<sub>3</sub>. Such results are probably attributed to the strong hydrogen bond network after BF<sub>4</sub> doping as mentioned above, which greatly strengthens the interactions between the organic and inorganic frameworks, thus gradually increasing the energy barrier for the dissociation process. The significant increase suggests that the tendency for decomposition into secondary phases of BF<sub>4</sub>-doped MAPbI<sub>3</sub> WBG perovskites is greatly suppressed, resulting in a considerable enhancement of its thermodynamic stability and facilitating the synthesis of the pure MAPbI<sub>3-x</sub>(BF<sub>4</sub>)<sub>x</sub> phase when compared to that of undoped MAPbI<sub>3</sub>.

To further evaluate the dynamic thermal stability within various systems at 300 K, the thermal atomic fluctuations are provided by the root-mean-square displacements (RMSDs) along the adiabatic MD trajectories. The MA, Pb, and I species are considered individually, and all results are summarized in Table I. It is noted that the thermal fluctuations

of the inorganic Pb and I ions, along with the organic cation MA, inversely correlate with BF<sub>4</sub> doping concentration. This relationship follows a clear sequence: 10% BF<sub>4</sub>-doped < 6% BF<sub>4</sub>-doped < 2% BF<sub>4</sub>-doped < pure MAPbI<sub>3</sub>. Such a trend provides further evidence that the thermal stability of perovskite is enhanced with increasing BF<sub>4</sub> doping concentration. Particularly, MA shows a more reduced thermal fluctuation. Its RMSD drops from 1.743 to 1.434 Å after only a slight (2%) BF<sub>4</sub> doping, about an 18% reduction, which is much larger than that of Pb (4%) and I (9%). Further analysis indicates that the greatly reduced thermal fluctuation of MA molecules mainly comes from their suppressed rotations. Plenty of works [60–62] have demonstrated MA molecules can freely rotate in MAPbI<sub>3</sub> perovskite. Here, pseudohalide BF<sub>4</sub> doping can effectively prohibit MA rotations as illustrated in Fig. S2 in the Supplemental Material [43] due to

TABLE I. RMSD in the position of MA, Pb, and I atoms along the MD trajectory in the pure, 2% BF<sub>4</sub>-doped, 6% BF<sub>4</sub>-doped, and 10% BF<sub>4</sub>-doped MAPbI<sub>3</sub> systems.

	Pb (Å)	I (Å)	MA (Å)
Pure MAPbI <sub>3</sub>	0.343	0.594	1.743
2% BF <sub>4</sub> -doped	0.328	0.538	1.434
6% BF <sub>4</sub> -doped	0.316	0.509	1.359
10% BF <sub>4</sub> -doped	0.315	0.462	1.292

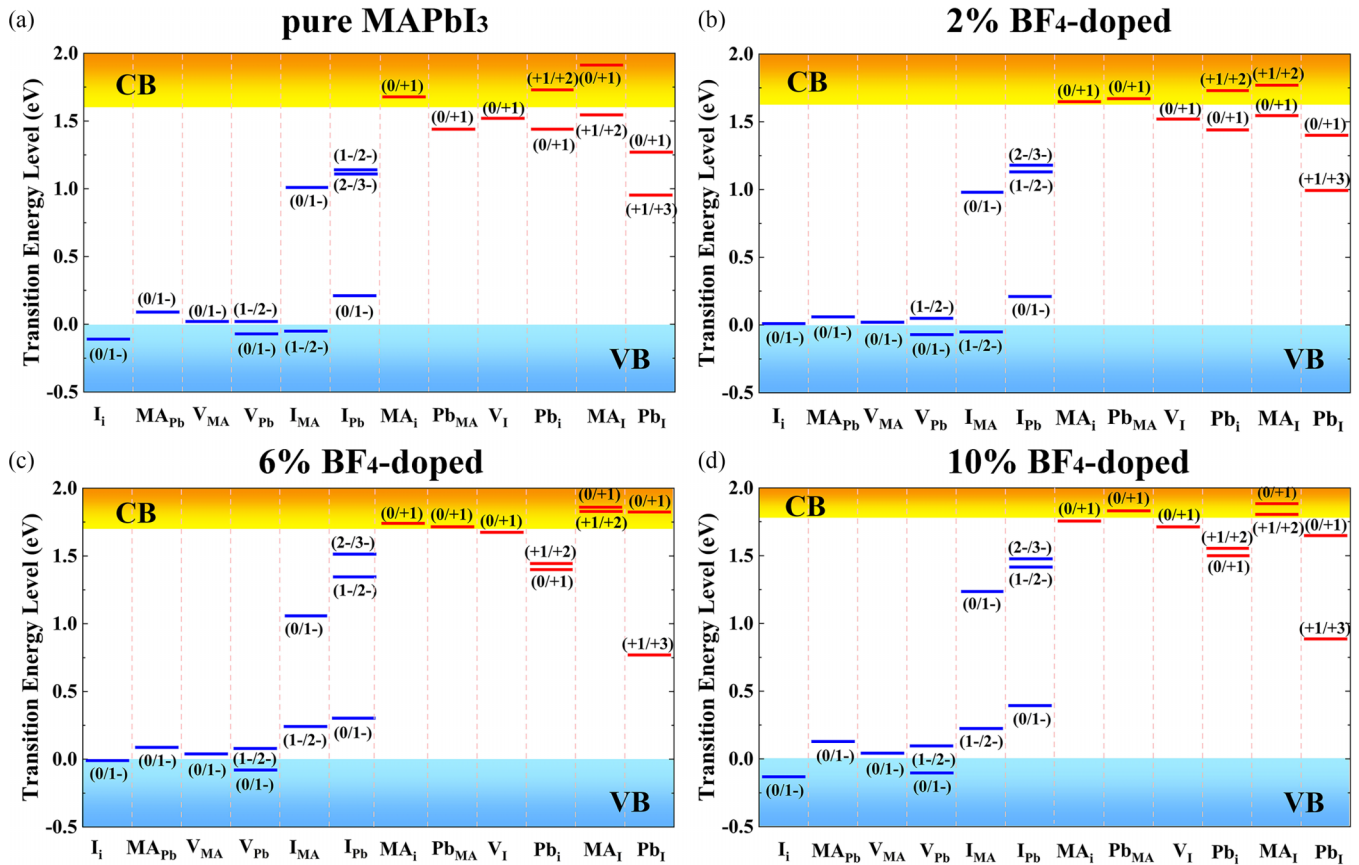


FIG. 3. The transition energy levels of intrinsic acceptors and intrinsic donors in (a) pure MAPbI<sub>3</sub>, (b) 2% BF<sub>4</sub>-doped MAPbI<sub>3</sub>, (c) 6% BF<sub>4</sub>-doped MAPbI<sub>3</sub>, and (d) 10% BF<sub>4</sub>-doped MAPbI<sub>3</sub>.

the strengthened hydrogen bond network as explained before. The suppressed MA rotations in BF<sub>4</sub>-doped perovskite once again confirm its enhanced rigidity and reduced anharmonicity. Therefore, BF<sub>4</sub>-doped WBG perovskites, particularly for 10% BF<sub>4</sub>-doped MAPbI<sub>3</sub>, exhibit enhanced thermal and phase stability when compared to undoped MAPbI<sub>3</sub> perovskite, which is beneficial for WBG PSC applications.

Defects play another important role in determining the stability and efficiency of solar cell materials, particularly because they act as traps and nonradiative recombination centers that shorten charge carrier lifetime and the long-term stability of perovskites [63–65]. To investigate defect behavior in MAPbI<sub>3-x</sub>(BF<sub>4</sub>)<sub>x</sub> perovskite, all potential intrinsic point defects close to BF<sub>4</sub> molecules (no longer than 3.6 Å) have been considered, including three vacancies (V<sub>MA</sub>, V<sub>Pb</sub>, V<sub>I</sub>), three interstitials (MA<sub>i</sub>, Pb<sub>i</sub>, I<sub>i</sub>), two cation substitutions (MA<sub>Pb</sub>, Pb<sub>MA</sub>), and four antisite substitutions (MA<sub>i</sub>, Pb<sub>i</sub>, I<sub>MA</sub>, I<sub>Pb</sub>). The defect formation energies for all intrinsic defects under different chemical environments are detailed in Table S1 of the Supplemental Material [43]. The charge transition levels for various charged defect states in the four systems were determined by Eq. (2), as depicted in Fig. 3. Figure 3(a) shows that most defects in MAPbI<sub>3</sub> generate shallow levels, which do not create additional recombination channels, agreeing well with previous simulation works [66–68]. It can be noted that MA<sub>i</sub>, Pb<sub>MA</sub>, V<sub>I</sub>, and MA<sub>i</sub> are shallow donors, while I<sub>i</sub>, MA<sub>Pb</sub>, V<sub>MA</sub>, and V<sub>Pb</sub> are shallow acceptors. These defects are still benign to MAPbI<sub>3</sub> perovskites although they

can widely exist with low formation energies. As for the rest of the point defects, although they generate deep gap states in some cases, they have high formation energies so their concentrations are expected to be low in OIHPs. The benign shallow intrinsic defects remain after BF<sub>4</sub> doping as demonstrated in Figs. 3(b)–3(d), with most of the transition energy levels changing by no more than 0.03 eV. All results clearly indicate that the equilibrated BF<sub>4</sub>-doped WBG perovskites should maintain the high defect tolerance as in pure MAPbI<sub>3</sub> perovskites, which could facilitate their high stability and slow nonradiative recombination.

Now we know that high defect tolerance can still be achieved in the equilibrated structure of BF<sub>4</sub>-doped WBG perovskites. However, previous work [69] has demonstrated that defects, considered to be benign, can become very detrimental under nonequilibrium conditions such as during ion migration. Among all the ions, the iodide ion migration has been widely observed in plenty of experimental studies [70–72] due to its lowest migration barrier, with an average value of around 0.44 eV [73]. Therefore, the iodine (along with iodine vacancy V<sub>I</sub>) migration has been studied in BF<sub>4</sub>-doped perovskites and compared with that in undoped MAPbI<sub>3</sub>, as shown in Fig. 4(a). In our previous work [74], the calculated activation energy barrier of iodine migration in pure MAPbI<sub>3</sub> perovskite is 0.40 eV, as shown in Fig. 4(b). After doping a small amount of BF<sub>4</sub>, the diffusion barrier for iodide ions migrating towards BF<sub>4</sub> molecules increases to 0.71 eV for 2% BF<sub>4</sub>-doped MAPbI<sub>3</sub> perovskite, 0.73 eV for 6% BF<sub>4</sub>-doped

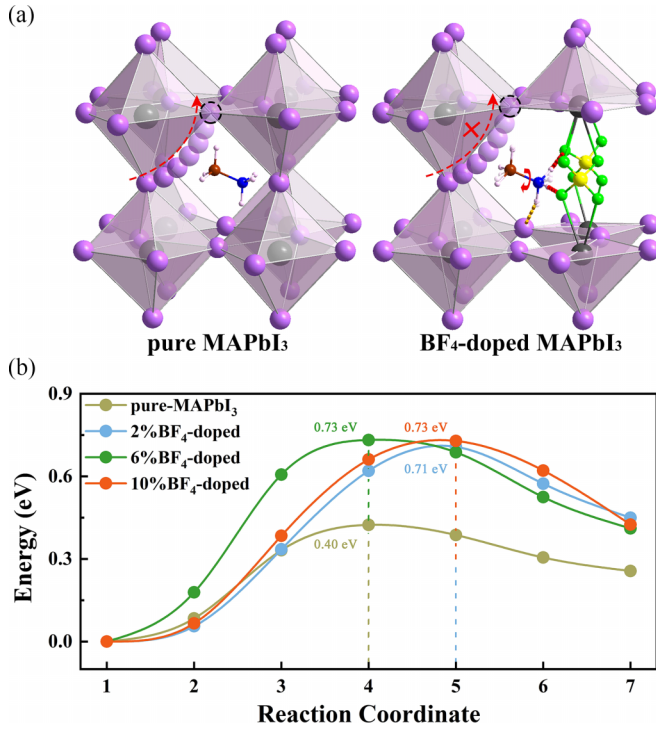


FIG. 4. (a) The schematic diagram of iodine ion diffusion in pure and BF<sub>4</sub>-doped MAPbI<sub>3</sub> systems. (b) The activation energy barriers for iodine ion diffusion in the pure MAPbI<sub>3</sub>, 2% BF<sub>4</sub>-doped MAPbI<sub>3</sub>, 6% BF<sub>4</sub>-doped MAPbI<sub>3</sub>, and 10% BF<sub>4</sub>-doped MAPbI<sub>3</sub> systems.

MAPbI<sub>3</sub> perovskite, and 0.73 eV for 10% BF<sub>4</sub>-doped MAPbI<sub>3</sub> perovskite, as illustrated in Fig. 4(b). The diffusion barrier increases by more than 78% after a small amount of BF<sub>4</sub> doping, suggesting an effective suppression of ion migration.

The mitigated ion migration in BF<sub>4</sub>-doped MAPbI<sub>3</sub> perovskite can be easily understood. The prevalent ion migration in perovskites mainly comes from their soft lattice structure and large inner space. Our previous work [75] has clarified that a small amount of BF<sub>4</sub> doping significantly reduces anharmonicity and enhances lattice rigidity. Furthermore, the larger effective ion radius of BF<sub>4</sub> molecules, in comparison to iodine atoms, results in spatial constriction. Moreover, doping with BF<sub>4</sub> leads to the formation of strong hydrogen bonds as clearly explained above, which can further compress the perovskite inner space. In addition, these strong hydrogen bonds around BF<sub>4</sub> are associated with the reorientation of the MA<sup>+</sup>, which consequently changes the distribution of strong molecular dipoles of MA<sup>+</sup>. It has been demonstrated that negative I ion migration is strongly inhibited when diffusing along the dipole direction of MA<sup>+</sup> [74]. In a word, the increased lattice rigidity, the confined inner space, and the reorientated dipole direction synergistically suppress the ion migration in BF<sub>4</sub>-doped MAPbI<sub>3</sub> perovskite. It should be pointed out that the iodine diffusion occurring far from BF<sub>4</sub> molecules remains unchanged as detailed in Fig. S3 in the Supplemental Material [43]. Therefore, delocalized doping of BF<sub>4</sub> in MAPbI<sub>3</sub> perovskite should be an effective way to inhibit ion migration, which in turn suppresses the common issue of phase separation in halogen-doped WBG perovskites, thereby enhancing the stability of WBG PSCs.

TABLE II. Band gap, average absolute NAC, and nonradiative  $e-h$  recombination time ( $\tau$ ) in four MAPbI<sub>3-x</sub>(BF<sub>4</sub>)<sub>x</sub> systems.

System	Band gap (eV)	NAC (meV)	$\tau$ (ns)
Pure MAPbI <sub>3</sub>	1.60	2.31	0.44
2% BF <sub>4</sub> -doped	1.63	1.93	0.79
6% BF <sub>4</sub> -doped	1.70	1.72	1.15
10% BF <sub>4</sub> -doped	1.78	1.21	3.45

Apart from the stability issues, another challenge for the performance of WBG PSCs is the limited diffusion length [76], which is determined by the charge carrier lifetime. In general, slow recombination rates (long lifetime) are associated with long diffusion lengths [77]. Moreover, previous experimental and theoretical studies [69,78,79] have established the fact that ion migration introduces a trap state into the fundamental energy gap, thereby accelerating the nonradiative  $e-h$  recombination. As mentioned above, BF<sub>4</sub> doping can effectively inhibit ion migration. Therefore, it is of great significance to investigate the nonradiative carrier recombination process under the impact of BF<sub>4</sub> doping on MAPbI<sub>3</sub> perovskite. Based on NAMD simulations, Fig. 5(a) illustrates the time-dependent population decay of the excited state involved in  $e-h$  recombination dynamics for pristine and BF<sub>4</sub>-doped (2%, 6%, 10%) MAPbI<sub>3</sub> systems. To determine the carrier recombination time  $\tau$ , we employ the short-time linear approximation to the exponential decay, given by  $P(t) = \exp(-t/\tau) \approx 1 - t/\tau$ . The relaxation times for nonradiative  $e-h$  recombination are 0.44 ns (pristine), 0.79 ns (2% BF<sub>4</sub>-doped), 1.15 ns (6% BF<sub>4</sub>-doped), and 3.45 ns (10% BF<sub>4</sub>-doped), as collected in Fig. 5(a) and Table II. All results reveal a significant increase in charge carrier lifetime with BF<sub>4</sub> doping concentrations up to 10%.

To elucidate the mechanisms underlying the significantly enhanced carrier lifetime in BF<sub>4</sub>-doped perovskites, the NAC between the conduction band minimum (CBM) and VBM is carefully analyzed because previous studies [80–84] have demonstrated the  $e-h$  recombination process is strongly dependent on the NAC. The NAC between adiabatic orbitals  $j$  and  $k$  is defined by  $-i\hbar\langle\phi_j|\nabla_R|\phi_k\rangle\frac{dR}{dt}$ . The first term characterizes the coupling between adiabatic orbitals due to the nuclear coordinate  $R$ , while the second term represents the corresponding nuclear velocity. Normally, a large NAC would result in a fast electron transition. As shown in Table II, the NAC value has decreased by nearly half from 2.31 meV in pure MAPbI<sub>3</sub> to 1.21 meV in 10% BF<sub>4</sub>-doped MAPbI<sub>3</sub>, which clearly explains the suppressed  $e-h$  recombination after BF<sub>4</sub> doping. To further understand details of NACs in BF<sub>4</sub>-doped MAPbI<sub>3</sub> WBG perovskites, Figs. 5(b)–5(e) illustrate matrices of the average absolute NACs between the electronic orbitals involved in the photoinduced charge transfer processes, including the electron transfer ( $e^-$  transfer: from CBM + 4 to CBM + 1),  $e-h$  recombination (from CBM to VBM), and hole transfer ( $h^+$  transfer: from VBM-1 to VBM-4); they are highlighted by orange, purple, and blue dashed lines, respectively. One can see the NACs in all BF<sub>4</sub>-doped systems are weaker than that in the undoped system, particularly for the  $e-h$  recombination and  $e^-$  transfer processes.

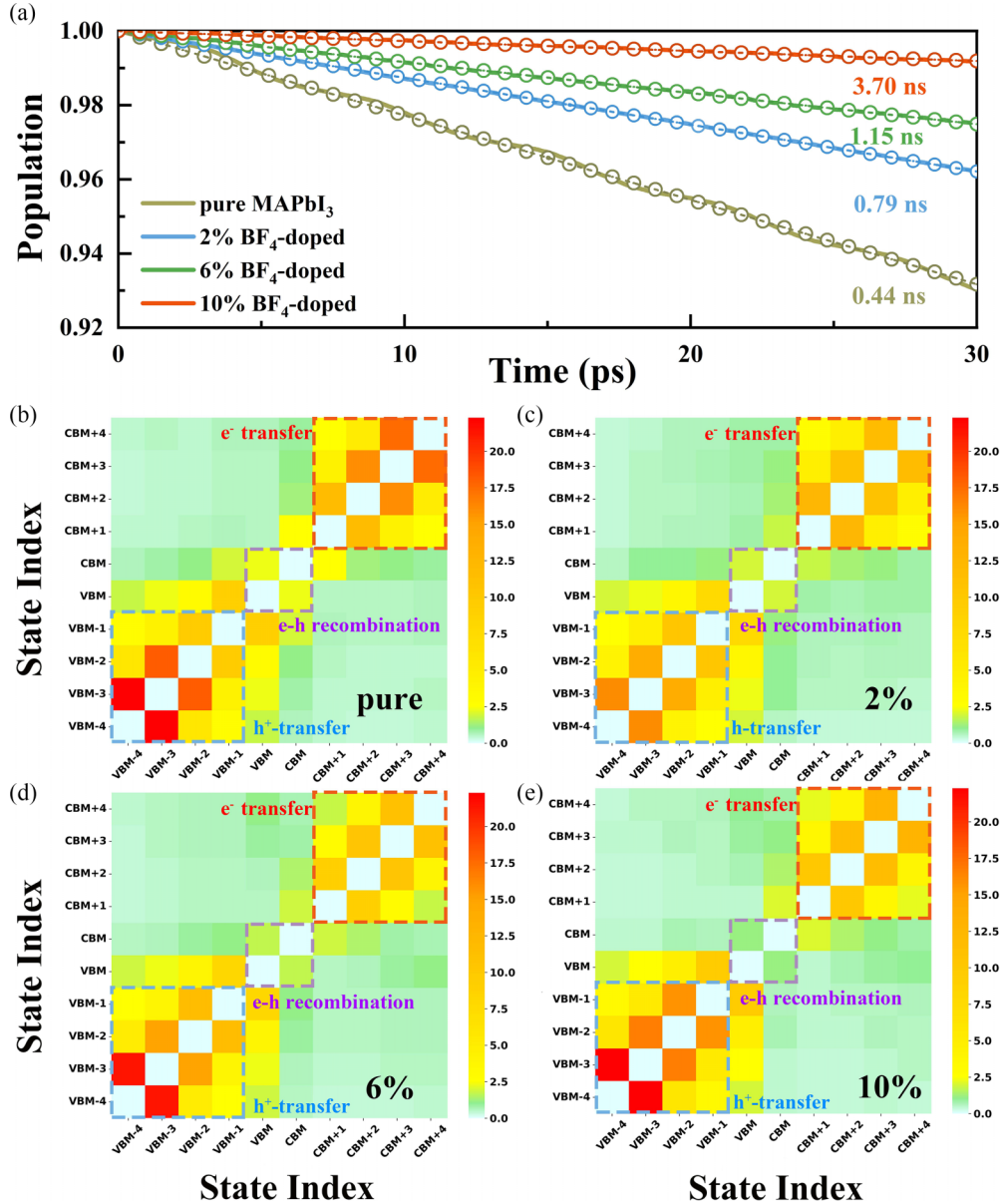


FIG. 5. (a) Nonradiative  $e-h$  recombination dynamics of  $\text{MAPbI}_{3-x}(\text{BF}_4)_x$  and averaged absolute magnitudes of the nonadiabatic couplings (meV) for the electron and hole transfer dynamics in (b) pure  $\text{MAPbI}_3$ , (c) 2%  $\text{BF}_4$ -doped  $\text{MAPbI}_3$ , (d) 6%  $\text{BF}_4$ -doped  $\text{MAPbI}_3$ , and (e) 10%  $\text{BF}_4$ -doped  $\text{MAPbI}_3$ . The color bar suggests the coupling strength: the red and green colors mean the strong and weak coupling strengths, respectively.

Specifically, the NAC value between the CBM and VBM decreases with increasing  $\text{BF}_4$  concentration, gradually changing from 2.31 meV (yellow) of the undoped system in Fig. 5(b) to 1.21 meV (green) of the 10%  $\text{BF}_4$ -doped system in Fig. 5(e) as mentioned above. This can be well understood. On the one hand, as the concentration of  $\text{BF}_4$  doping increases, the atomic fluctuations are significantly reduced, as proved by lower RMSD values in Table I. On the other hand, our previous work [75] has shown that a small amount of  $\text{BF}_4$  doping effectively reduces the anharmonicity of inorganic Pb and I atoms, and suppresses the vibrations of the MA molecules. This leads to weakened electron-phonon interactions and introduces small NAC values. In addition, the NACs in the electron transfer [orange dashed boxes in Figs. 5(b)–5(e)] are significantly suppressed after doping a small amount of  $\text{BF}_4$ .

As discussed in previous works [85,86], the HC cooling rate is dependent on the NAC. Generally, the small NAC indicates a slow HC cooling process. Thus, our results show that  $\text{BF}_4$ -doped systems can also efficiently slow down hot electron cooling and avoid accelerating hot hole cooling compared to pure  $\text{MAPbI}_3$ , which is promising for the development of HC solar cells. Finally, it can be concluded that the reduced NAC in the  $\text{BF}_4$ -doped WBG perovskites can extend the charge carrier lifetime and improve the photovoltaic performance when compared to the pure  $\text{MAPbI}_3$  perovskite.

#### IV. CONCLUSION

In summary, using *ab initio* time-independent and real-time time-dependent DFT, coupled with NAMD, we have

investigated thermal stability, defect levels, ion migration, and nonradiative recombination in the low concentration  $\text{BF}_4$ -doped  $\text{MAPbI}_3$  WBG perovskite. Our study demonstrated that the doped pseudohalide  $\text{BF}_4$  not only introduces strong N–H...F hydrogen bonds, but also strengthens the adjacent N–H...I hydrogen bonds. As a result, a comprehensively strengthened hydrogen bond network is formed in  $\text{BF}_4$ -doped perovskite, which enhances the lattice rigidity and prohibits the rotation of MA molecules along the adiabatic MD trajectories. A small amount of  $\text{BF}_4$  doping would dramatically increase the dissociation energy to 0.64 eV, an order of magnitude larger than that (0.015 eV) in pure  $\text{MAPbI}_3$  perovskite. Along with the reduced thermal atomic fluctuation,  $\text{BF}_4$ -doped WBG perovskites exhibit greatly enhanced thermodynamic stability and they do not introduce additional deep energy level defects so the high defect tolerance characteristic is maintained as in pure  $\text{MAPbI}_3$  perovskite. Furthermore,  $\text{BF}_4$  doping can reduce the anharmonicity of the soft inorganic lattice, introduce the spatial confinement effect, and induce the reorientation of dipole direction due to MA molecules, which synergistically suppress the most popular iodine migration, inhibiting the common issue of phase separation in halogen-doped WBG perovskites. Moreover, both nonradiative  $e$ – $h$  recombination and hot carrier cooling processes are greatly inhibited as well after  $\text{BF}_4$  doping mainly due to the significantly decreased NAC values. As a result, the charge

carrier lifetime of  $\text{BF}_4$ -doped  $\text{MAPbI}_3$  WBG perovskite is an order of magnitude longer than that of pure  $\text{MAPbI}_3$ . Finally, a 10% delocalized  $\text{BF}_4$ -doped  $\text{MAPbI}_3$  would be particularly beneficial when applied to WBG PSCs. Our findings highlight the importance of fluorinated pseudohalide  $\text{BF}_4$  doping strategies in WBG perovskite materials to achieve improved stability and efficiency, offering a promising approach for future research and development in photovoltaic technologies.

## ACKNOWLEDGMENTS

This work was financially supported by the National Key Research and Development Program of China (Grant No. 2022YFB4200501), the National Natural Science Foundation of China (Grants No. 12104515 and No. 52073308), the Central South University Research Program of Advanced Interdisciplinary Studies (Grant No. 2023QYJC013), Key programs of Xinjiang Natural Science Foundation (Grant No. 2022B02051), and the Tianshan Innovation Team Program of Xinjiang Uygur Autonomous Region (Grant No. 2023D14001). We are grateful for resources from the High-Performance Computing Center of Central South University. We also acknowledge resources from the Hefei Advanced Computing Center.

The authors declare no competing financial interest.

- 
- [1] A. Kojima, K. Teshima, Y. Shirai, and T. Miyasaka, *J. Am. Chem. Soc.* **131**, 6050 (2009).
- [2] E. Menéndez-Proupin, P. Palacios, P. Wahnón, and J. C. Conesa, *Phys. Rev. B* **90**, 045207 (2014).
- [3] F. Brivio, J. M. Frost, J. M. Skelton, A. J. Jackson, O. J. Weber, M. T. Weller, A. R. Goñi, A. M. A. Leguy, P. R. F. Barnes, and A. Walsh, *Phys. Rev. B* **92**, 144308 (2015).
- [4] A. C. Ferreira, A. Létoublon, S. Paofai, S. Raymond, C. Ecolivet, B. Rufflé, S. Cordier, C. Katan, M. I. Saidaminov, A. A. Zhumekenov *et al.*, *Phys. Rev. Lett.* **121**, 085502 (2018).
- [5] G. Yang, Z. Ren, K. Liu, M. Qin, W. Deng, H. Zhang, H. Wang, J. Liang, F. Ye, Q. Liang *et al.*, *Nat. Photonics* **15**, 681 (2021).
- [6] J.-W. Lee, S. Tan, S. I. Seok, Y. Yang, and N.-G. Park, *Science* **375**, eabj1186 (2022).
- [7] J. Park, J. Kim, H.-S. Yun, M. J. Paik, E. Noh, H. J. Mun, M. G. Kim, T. J. Shin, and S. I. Seok, *Nature (London)* **616**, 724 (2023).
- [8] R. Lin, Y. Wang, Q. Lu, B. Tang, J. Li, H. Gao, Y. Gao, H. Li, C. Ding, J. Wen *et al.*, *Nature (London)* **620**, 994 (2023).
- [9] H. Lin, M. Yang, X. Ru, G. Wang, S. Yin, F. Peng, C. Hong, M. Qu, J. Lu, L. Fang *et al.*, *Nat. Energy* **8**, 789 (2023).
- [10] J. Zhou, X. Xu, H. Wu, J. Wang, L. Lou, K. Yin, Y. Gong, J. Shi, Y. Luo, D. Li *et al.*, *Nat. Energy* **8**, 526 (2023).
- [11] S. Martani, Y. Zhou, I. Poli, E. Aktas, D. Meggiolaro, J. Jiménez-López, E. L. Wong, L. Gregori, M. Prato, and D. Di Girolamo, *ACS Energy Lett.* **8**, 2801 (2023).
- [12] F. Peña-Camargo, P. Caprioglio, F. Zu, E. Gutierrez-Partida, C. M. Wolff, K. Brinkmann, S. Albrecht, T. Riedl, N. Koch, and D. Neher, *ACS Energy Lett.* **5**, 2728 (2020).
- [13] E. T. Hoke, D. J. Slotcavage, E. R. Dohner, A. R. Bowring, H. I. Karunadasa, and M. D. McGehee, *Chem. Sci.* **6**, 613 (2015).
- [14] A. J. Barker, A. Sadhanala, F. Deschler, M. Gandini, S. P. Senanayak, P. M. Pearce, E. Mosconi, A. J. Pearson, Y. Wu, and A. R. Srimath Kandada, *ACS Energy Lett.* **2**, 1416 (2017).
- [15] Y. Zhou, Y. H. Jia, H. H. Fang, M. A. Loi, F. Y. Xie, L. Gong, M. C. Qin, X. H. Lu, C. P. Wong, and N. Zhao, *Adv. Funct. Mater.* **28**, 1803130 (2018).
- [16] U.-G. Jong, C.-J. Yu, J.-S. Ri, N.-H. Kim, and G.-C. Ri, *Phys. Rev. B* **94**, 125139 (2016).
- [17] F. Xu, M. Zhang, Z. Li, X. Yang, and R. Zhu, *Adv. Energy Mater.* **13**, 2203911 (2023).
- [18] Z. Zhang, J. Wang, J. Liang, Y. Zheng, X. Wu, C. Tian, A. Sun, Y. Huang, Z. Zhou, Y. Yang *et al.*, *Small* **19**, 2303213 (2023).
- [19] T. Nie, J. Yang, Z. Fang, Z. Xu, X. Ren, X. Guo, T. Chen, and S. F. Liu, *Chem. Eng. J.* **468**, 143341 (2023).
- [20] C. Su, R. Wang, J. Tao, J. Shen, D. Wang, L. Wang, G. Fu, S. Yang, M. Yuan, and T. He, *J. Mater. Chem. A* **11**, 6565 (2023).
- [21] J. Tao, X. Liu, J. Shen, S. Han, L. Guan, G. Fu, D.-B. Kuang, and S. Yang, *ACS Nano* **16**, 10798 (2022).
- [22] A. Kumar, K. R. Balasubramaniam, J. Kangsabanik, Vikram, and A. Alam, *Phys. Rev. B* **94**, 180105(R) (2016).
- [23] Z. Li, Z. Li, G. Peng, C. Shi, H. Wang, S.-Y. Ding, Q. Wang, Z. Liu, and Z. Jin, *Adv. Mater.* **35**, 2300480 (2023).
- [24] J. Zhang, S. Wu, T. Liu, Z. Zhu, and A. K. Y. Jen, *Adv. Funct. Mater.* **29**, 1808833 (2019).
- [25] H. Cheng, C. Liu, J. Zhuang, J. Cao, T. Wang, W. Y. Wong, and F. Yan, *Adv. Funct. Mater.* **32**, 2204880 (2022).
- [26] J. Koh, D. Kim, S. W. Park, H. Kim, K.-H. Hong, and B. Shin, *J. Mater. Chem. A* **12**, 4290 (2024).



- [27] G. Kresse and J. Furthmüller, *Phys. Rev. B* **54**, 11169 (1996).
- [28] J. P. Perdew, K. Burke, and M. Ernzerhof, *Phys. Rev. Lett.* **77**, 3865 (1996).
- [29] P. E. Blöchl, *Phys. Rev. B* **50**, 17953 (1994).
- [30] G. Henkelman and H. Jónsson, *J. Chem. Phys.* **113**, 9978 (2000).
- [31] G. Henkelman, B. P. Uberuaga, and H. Jónsson, *J. Chem. Phys.* **113**, 9901 (2000).
- [32] S. Grimme, J. Antony, S. Ehrlich, and H. Krieg, *J. Chem. Phys.* **132**, 154104 (2010).
- [33] S. Grimme, S. Ehrlich, and L. Goerigk, *J. Comput. Chem.* **32**, 1456 (2011).
- [34] H. M. Jaeger, S. Fischer, and O. V. Prezhdo, *J. Chem. Phys.* **137**, 22A545 (2012).
- [35] A. V. Akimov and O. V. Prezhdo, *J. Chem. Theory Comput.* **9**, 4959 (2013).
- [36] A. V. Akimov and O. V. Prezhdo, *J. Chem. Theory Comput.* **10**, 789 (2014).
- [37] A.-Y. Zhu, R.-X. Ding, H.-T. Xu, C.-J. Tong, and K. P. McKenna, *ACS Energy Lett.* **9**, 497 (2024).
- [38] N.-J. Hao, R.-X. Ding, C.-J. Tong, and K. P. McKenna, *J. Appl. Phys.* **133**, 145002 (2023).
- [39] Y. Liu, R. Long, W.-H. Fang, and O. V. Prezhdo, *J. Am. Chem. Soc.* **145**, 14112 (2023).
- [40] T.-F. Lu, W. Chu, S. Agrawal, Z. Zhang, and O. V. Prezhdo, *J. Phys. Chem. Lett.* **14**, 10685 (2023).
- [41] S. Gumber, O. Eniodunmo, S. A. Ivanov, S. Kilina, O. V. Prezhdo, D. Ghosh, and S. Tretiak, *J. Mater. Chem. A* **11**, 8256 (2023).
- [42] R. Esteban-Puyuelo and B. Sanyal, *Phys. Rev. B* **103**, 235433 (2021).
- [43] See Supplemental Material at <http://link.aps.org/supplemental/10.1103/PhysRevB.110.045142> for the theory details, details of MAPb[I<sub>(1-x)</sub>(BF<sub>4</sub>)<sub>x</sub>]<sub>3</sub> structure, optimized structures of BF<sub>4</sub>-doped systems, the net dipole moment orientation ratios in all BF<sub>4</sub>-doped MAPbI<sub>3</sub> perovskites, defect formation energies of BF<sub>4</sub>-doped systems, and NEB calculations on iodine migration which occurs far from BF<sub>4</sub> molecules in all BF<sub>4</sub>-doped MAPbI<sub>3</sub> perovskites. It also contains Refs. [44–49].
- [44] Z. Wang, Z. Zheng, Q. Zheng, and J. Zhao, *J. Phys. Chem. Lett.* **15**, 3907 (2024).
- [45] W. Li, R. Long, J. Tang, and O. V. Prezhdo, *J. Phys. Chem. Lett.* **10**, 3788 (2019).
- [46] Z. Zheng, Y. Shi, J.-J. Zhou, O. V. Prezhdo, Q. Zheng, and J. Zhao, *Nat. Comput. Sci.* **3**, 532 (2023).
- [47] X. Jiang, Q. Zheng, Z. Lan, W. A. Saidi, X. Ren, and J. Zhao, *Sci. Adv.* **7**, eabf3759 (2021).
- [48] B. F. Habenicht and O. V. Prezhdo, *Phys. Rev. Lett.* **100**, 197402 (2008).
- [49] S. V. Kilina, A. J. Neukirch, B. F. Habenicht, D. S. Kilin, and O. V. Prezhdo, *Phys. Rev. Lett.* **110**, 180404 (2013).
- [50] S.-H. Wei and S. B. Zhang, *Phys. Rev. B* **66**, 155211 (2002).
- [51] S. B. Zhang, S.-H. Wei, and A. Zunger, *Phys. Rev. B* **63**, 075205 (2001).
- [52] S. Nagane, S. Macpherson, M. A. Hope, D. J. Kubicki, W. Li, S. D. Verma, J. Ferrer Orri, Y.-H. Chiang, J. L. MacManus-Driscoll, C. P. Grey *et al.*, *Adv. Mater.* **33**, 2102462 (2021).
- [53] N. Li, S. Tao, Y. Chen, X. Niu, C. K. Onwudiantanti, C. Hu, Z. Qiu, Z. Xu, G. Zheng, L. Wang *et al.*, *Nat Energy* **4**, 408 (2019).
- [54] A. Yang, D. Li, X. Lai, H. Zhang, and C. Liang, *J. Phys. Chem. C* **125**, 21223 (2021).
- [55] L. Lin, T. W. Jones, T. C.-J. Yang, X. Li, C. Wu, Z. Xiao, H. Li, J. Li, J. Qian, L. Lin *et al.*, *Matter* **7**, 38 (2024).
- [56] S. Chen, Y. Zhang, X. Zhang, J. Zhao, Z. Zhao, X. Su, Z. Hua, J. Zhang, J. Cao, J. Feng *et al.*, *Adv. Mater.* **32**, 2001107 (2020).
- [57] W. Huang, S. Sadhu, and S. Ptasinska, *Chem. Mater.* **29**, 8478 (2017).
- [58] M. L. Agiorgousis, Y.-Y. Sun, H. Zeng, and S. Zhang, *J. Am. Chem. Soc.* **136**, 14570 (2014).
- [59] W. Ming, S. Chen, and M.-H. Du, *J. Mater. Chem. A* **4**, 16975 (2016).
- [60] O. Selig, A. Sadhanala, C. Muller, R. Lovrincic, Z. Chen, Y. L. Rezus, J. M. Frost, T. L. Jansen, and A. A. Bakulin, *J. Am. Chem. Soc.* **139**, 4068 (2017).
- [61] C. Motta, F. El-Mellouhi, S. Kais, N. Tabet, F. Alharbi, and S. Sanvito, *Nat. Commun.* **6**, 7026 (2015).
- [62] D. H. Fabini, T. A. Siaw, C. C. Stoumpos, G. Laurita, D. Olds, K. Page, J. G. Hu, M. G. Kanatzidis, S. Han, and R. Seshadri, *J. Am. Chem. Soc.* **139**, 16875 (2017).
- [63] D. Luo, R. Su, W. Zhang, Q. Gong, and R. Zhu, *Nat. Rev. Mater.* **5**, 44 (2020).
- [64] W. Shockley and W. Read, Jr., *Phys. Rev.* **87**, 835 (1952).
- [65] C.-J. Tong, X. Cai, A.-Y. Zhu, L.-M. Liu, and O. V. Prezhdo, *J. Am. Chem. Soc.* **144**, 6604 (2022).
- [66] W.-J. Yin, T. Shi, and Y. Yan, *Appl. Phys. Lett.* **104**, 063903 (2014).
- [67] W.-J. Yin, T. Shi, and Y. Yan, *J. Phys. Chem. C* **119**, 5253 (2015).
- [68] S. Yun, X. Zhou, J. Even, and A. Hagfeldt, *Angew. Chem., Int. Ed.* **56**, 15806 (2017).
- [69] C.-J. Tong, L. Li, L.-M. Liu, and O. V. Prezhdo, *J. Am. Chem. Soc.* **142**, 3060 (2020).
- [70] L. McGovern, M. H. Futscher, L. A. Muscarella, and B. Ehrler, *J. Phys. Chem. Lett.* **11**, 7127 (2020).
- [71] Y. Yuan and J. Huang, *Acc. Chem. Res.* **49**, 286 (2016).
- [72] P. V. Kamat and M. Kuno, *Acc. Chem. Res.* **54**, 520 (2021).
- [73] J. Haruyama, K. Sodeyama, L. Han, and Y. Tateyama, *J. Am. Chem. Soc.* **137**, 10048 (2015).
- [74] C.-J. Tong, W. Geng, O. V. Prezhdo, and L.-M. Liu, *ACS Energy Lett.* **2**, 1997 (2017).
- [75] Z.-Y. Wang, H.-Q. Ye, K.-F. Wang, F. Ouyang, Z. Wu, and C.-J. Tong, *Appl. Phys. Lett.* **123**, 183904 (2023).
- [76] J. Xu, C. C. Boyd, Z. J. Yu, A. F. Palmstrom, D. J. Witter, B. W. Larson, R. M. France, J. Werner, S. P. Harvey, E. J. Wolf *et al.*, *Science* **367**, 1097 (2020).
- [77] Y. Chen, H. T. Yi, X. Wu, R. Haroldson, Y. N. Gartstein, Y. I. Rodionov, K. S. Tikhonov, A. Zakhidov, X. Y. Zhu, and V. Podzorov, *Nat. Commun.* **7**, 12253 (2016).
- [78] M. Gerhard, B. Louis, R. Camacho, A. Merdasa, J. Li, A. Kiligaridis, A. Dobrovolsky, J. Hofkens, and I. G. Scheblykin, *Nat. Commun.* **10**, 1698 (2019).
- [79] S. D. Stranks, *ACS Energy Lett.* **2**, 1515 (2017).
- [80] W. Chu, Q. Zheng, O. V. Prezhdo, J. Zhao, and W. A. Saidi, *Sci. Adv.* **6**, eaaw7453 (2020).
- [81] L. Zhang, Q. Zheng, Y. Xie, Z. Lan, O. V. Prezhdo, W. A. Saidi, and J. Zhao, *Nano Lett.* **18**, 1592 (2018).
- [82] L. Zhang, Q. Wang, L. Wang, L. Wang, J. Zhao, and S. Li, *Phys. Rev. B* **109**, 075306 (2024).

- [83] L. Zhang, W. Chu, Q. Zheng, A. V. Benderskii, O. V. Prezhdo, and J. Zhao, *J. Phys. Chem. Lett.* **10**, 6151 (2019).
- [84] Q. Zheng, W. Chu, C. Zhao, L. Zhang, H. Guo, Y. Wang, X. Jiang, and J. Zhao, *WIREs Comput. Mol. Sci.* **9**, e1411 (2019).
- [85] J. Yin, P. Maity, R. Naphade, B. Cheng, J.-H. He, O. M. Bakr, J.-L. Brédas, and O. F. Mohammed, *ACS Nano* **13**, 12621 (2019).
- [86] M. E. Madjet, G. R. Berdiyrov, F. El-Mellouhi, F. H. Alharbi, A. V. Akimov, and S. Kais, *J. Phys. Chem. Lett.* **8**, 4439 (2017).